

LOW ENERGY SPECTRAL INDEX AND E_p EVOLUTION OF QUASI-THERMAL PHOTOSPHERE EMISSION OF GAMMA-RAY BURSTS

WEI DENG (邓巍), BING ZHANG (张冰)

Department of Physics and Astronomy, University of Nevada Las Vegas, Las Vegas, NV 89154, USA
deng@physics.unlv.edu, zhang@physics.unlv.edu

ABSTRACT

Recent observations by the Fermi satellite suggest that a photosphere emission component is contributing to the observed spectrum of many GRBs. One important question is whether the photosphere component can interpret the typical “Band” function of GRBs with a typical low energy photon spectral index $\alpha \sim -1$. We perform a detailed study of the photosphere emission spectrum by progressively introducing several physical ingredients previously not fully incorporated, including the probability distribution of the location of a dynamically evolving photosphere, superposition of emission from an equal-arrival-time “volume” in a continuous wind, the evolution of optical depth of a wind with finite but evolving outer boundary, as well as the effect of different top-hat wind luminosity (L_w) profiles. By assuming a co-moving blackbody spectrum emerging from the photosphere, we find that for an outflow with a constant or increasing L_w , the low-energy spectrum below the peak energy (E_p), can be modified to $F_\nu \sim \nu^{1.5}$ ($\alpha \sim +0.5$). A softer ($-1 < \alpha < +0.5$) or flat ($\alpha = -1$) spectrum can be obtained during the L_w decreasing phase or high-latitude-emission-dominated phase. We also study the evolution of E_p as a function of wind and photosphere luminosity in this photosphere model. An $E_p - L$ tracking pattern can be reproduced if a certain positive dependence between the dimensionless entropy η and L_w is introduced. However, the hard-to-soft evolution pattern cannot be reproduced unless a contrived condition is invoked. In order to interpret the Band spectrum, a more complicated photosphere model or a different energy dissipation and radiation mechanism are needed.

Subject headings: gamma-rays: bursts - radiation mechanisms: thermal - relativity

1. INTRODUCTION

Despite more than 40 years of observations of gamma-ray bursts (GRBs), the radiation mechanism during the prompt emission phase is still being debated. Observationally the time-resolved spectra are usually characterized by a smoothly-joint broken power law, known as the “Band” function (Band et al. 1993). The typical value of the low-energy photon spectral index α (the one below the peak energy E_p) is around -1 (Preece et al. 2000; Zhang et al. 2011; Nava et al. 2011)¹. This value is not straightforwardly predicted in available models. In general there are two broad categories of GRB prompt emission models, one invoking a Comptonized quasi-thermal emission from the photosphere of the outflow (Thompson 1994; Ghisellini & Celotti 1999; Mészáros & Rees 2000; Mészáros et al. 2002; Rees & Mészáros 2005; Pe’er et al. 2006; Thompson et al. 2007; Pe’er 2008; Giannios 2008; Beloborodov 2010; Lazzati & Begelman 2010; Ioka 2010; Toma et al. 2011; Pe’er & Ryde 2011; Mizuta et al. 2011; Lundman et al. 2013; Lazzati et al. 2013; Ruffini et al. 2013), the other invoking a non-thermal (synchrotron or synchrotron-self-Compton) mechanism in the optically thin region (Mészáros et al. 1994; Tavani 1996; Daigne & Mochkovitch 1998; Lloyd & Petrosian 2000; Zhang & Mészáros 2002a; Kumar & Panaitescu 2008; Zhang & Pe’er 2009;

Wang et al. 2009; Kumar & Narayan 2009; Daigne et al. 2011; Zhang & Yan 2011; Zhang et al. 2012; Veres et al. 2012; Burgess et al. 2011; Uhm & Zhang 2013). Recent observations with Fermi (Ryde et al. 2010; Zhang et al. 2011; Guiriec et al. 2011; Axelsson et al. 2012; Guiriec et al. 2013) confirmed the pre-Fermi suggestion (Ryde 2005; Ryde & Pe’er 2009) that the observed GRB spectra sometimes include superposition of a quasi-thermal component with a non-thermal component², suggesting that the photosphere emission indeed contributes to the observed GRB spectra of at least some GRBs. The question is how much the photosphere emission contributes to the observed spectra. There are two different opinions. According to the first opinion, only the quasi-thermal component identified in some GRBs is of the photosphere origin (e.g. Ryde et al. 2010; Zhang et al. 2011; Guiriec et al. 2011; Axelsson et al. 2012; Guiriec et al. 2013), while the main “Band” component is non-thermal emission from an optically thin region. The second, more optimistic opinion suggests that the main Band component is of a photosphere origin, and the observed E_p is defined by the photosphere temperature (e.g. Rees & Mészáros 2005; Thompson et al. 2007; Beloborodov 2010; Lazzati & Begelman 2010; Pe’er & Ryde 2011; Lundman et al. 2013; Lazzati et al. 2013).

Within this second scenario, one needs to broaden the quasi-thermal spectrum to a mimic the observed “Band” function. The high-energy photon index can be eas-

¹ Some GRBs show a harder α value in the time resolved spectra at the beginning or around the peak of the light curve (Ghirlanda et al. 2002, 2003). In some other cases, a blackbody component can play a dominant role (Ryde et al. 2010; Zhang et al. 2011; Ghirlanda et al. 2013).

² Observational constraints demand that non-thermal component cannot be a single power law extending to much lower energies (Ghirlanda et al. 2007).

ily interpreted by introducing dissipation of energy near photosphere so that non-thermal electrons are accelerated to upscatter the seed quasi-thermal photons (e.g. Lazzati & Begelman 2010). However, the main difficulty is to account for the observed low-energy photon index $\alpha \sim -1$, since the predicted value is much harder than this value (e.g. Beloborodov 2010). It has been speculated that geometric smearing and temporal smearing may soften the spectrum to make α closer to -1, but no thorough study has been carried out.

Another interesting observational feature is the E_p evolution in GRBs. Observationally two patterns are identified: hard-to-soft evolution or E_p -intensity tracking (Liang & Kargatis 1996; Ford et al. 1995; Ghirlanda et al. 2010, 2011a,b; Lu et al. 2010, 2012) across a broad GRB pulse (or the “slow” variability component, Gao et al. 2012). Various data analyses suggest that both patterns co-exist, sometimes in a same burst. For short GRBs, the tracking behavior is most common, while for long GRBs, especially for the first broad pulse, the hard-to-soft evolution is relatively more common (e.g. Preece et al. 2014). Simulations show that in long GRBs, tracking pulses after the first pulse could be due to a superposition of multiple hard-to-soft pulses (Lu et al. 2012), and it has been argued that the hard-to-soft evolution pattern may be ubiquitous among long GRBs (Hakkila & Preece 2011, 2014). It is of great interest to see what E_p evolution pattern the photosphere model predicts.

In this paper, we investigate the predictions of α values and E_p evolutions within the simplest photosphere model (a co-moving blackbody spectrum and a uniform jet) by fully treating the geometrical and temporal smearing effects. In Sect.2, we describe our methodology, in particular, improvements upon previous work. We then present calculations of photosphere spectra and E_p evolution patterns in progressively more complicated models in Sect.3. The conclusions are drawn in Sect.4.

2. METHODOLOGY

2.1. Previous work on probability photosphere model

Photosphere may be roughly defined as a radius at which the Thomson scattering optical depth for a photon is $\tau = 1$. From the microscopic view, an individual photon in the outflow can be in principle last scattered by an electron at any position with a certain probability. One should introduce a probability function to describe photosphere emission (Pe’er 2008; Pe’er & Ryde 2011; Beloborodov 2011). In general, for a group of photons emerging from deep inside the photosphere, they can undergo last scattering at any location (r, Ω) inside the outflow, where r is the radius from the explosion center, and $\Omega(\theta, \phi)$ defines the angular coordinates. A probability function $P(r, \Omega)$ is introduced to describe the chance of last scattering at any location.

So far, a most detailed treatment of the probability function was presented in Pe’er (2008), Pe’er & Ryde (2011) and Beloborodov (2011). By making some simplifications in modeling, their model caught the essence of the photospheric physics. The basic physical picture of Pe’er & Ryde (2011) can be summarized as follows (see the cartoon picture Figure 1a): The central engine remains active for a while and forms a conical outflow. Af-

ter some time the central engine is shut down. They assumed that the wind luminosity L_w , the initial mass loss rate \dot{M} , and hence, the initial bulk lorentz factor Γ , are all constant. This means that a continuous wind with a time-independent density profile is established. For simplicity, they also assumed that such a wind extends to an infinite distance. As a result, the optical depth could be directly calculated by an analytical formula, which is time-independent (Pe’er 2008; Pe’er & Ryde 2011). Another simplification of Pe’er & Ryde (2011) is that they only considered an instantaneous deposition of photons in one thin layer at the center of an expanding outflow plasma. In reality, photons are continuously deposited into a series of layers ejected by a long-lasting central engine. This would make calculations more complicated. A third simplification in their analytical approach is that they assumed a mono-energetic photon field, while in reality the photons have a distribution (e.g. blackbody in the co-moving frame). This assumption was removed in their numerical approach through Monte Carlo simulations. In any case, an analytical approach to handle the blackbody spectrum is welcome.

2.2. Improvements

In order to give a more precise treatment on more realistic situations, in this paper we make several critical improvements on the previous work to establish a more sophisticated photosphere model to study the instantaneous and time-integrated spectra and E_p evolution by allowing a time-varying central engine wind, and hence, the optical depth. Our improvements on the previous work include the following: 1. We introduce a blackbody distribution of the photons in the comoving frame, to replace the mono-energetic photon distribution in the analytical treatment of Pe’er (2008) and Pe’er & Ryde (2011); 2. For a wind lasting for a certain duration, at any instant, photons from different layers and latitudes, which were emitted at different epochs, are received. Instead of the traditional “equal-arrival-time-surface” effect commonly considered in an afterglow model, one needs to consider “equal-arrival-time-volume” for a more precise treatment of the photosphere emission. We separate the outflow into many thin layers, follow the last scattering of electrons from each layer individually, and calculate the sum of flux from all the layers from different latitudes and emission times, but at a same observer time; 3. We introduce a finite, dynamically evolving front of the outflow based on the assumed injection history of the outflow. This would affect the calculation of the Thomson scattering optical depth of the photons, which leads to a more precise derivation of the photosphere radius in different directions. The effect is especially important in the early phase of the outflow; 4. Since GRB lightcurves show an erratic behavior, we introduce time-dependent wind luminosity and baryon loading to allow a more realistic treatment of time-variable photosphere emission.

A cartoon picture of our improved model is shown in Fig.1b, as compared with Fig.1a. Due to the finite central engine activity time, the outflow has a finite thickness. We separate the outflow into many thin layers, each characterized by an initial wind luminosity L_w and an initial mass loading rate \dot{M} . To treat the equal-arrival-

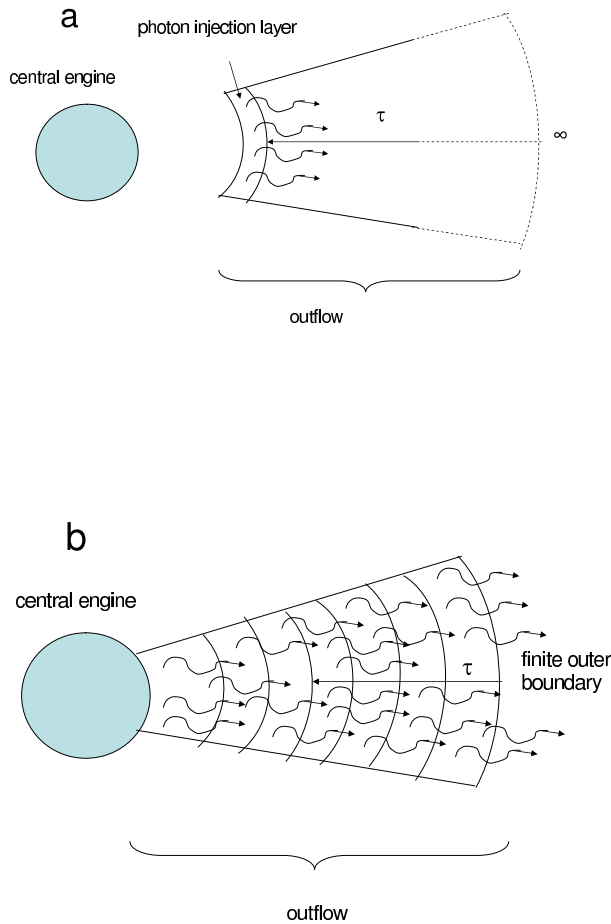


FIG. 1.— The cartoon picture for the model of Pe’er (2008); Pe’er & Ryde (2011) (a) as compared with ours (b).

time volume effect, we consider two levels of integration. The first level handles the equal-arrival-time surface of each layer: photons emitted from different latitudes at different times arrive the observer at the same time; The second level handles superposition of emission from different layers: high-latitude emission from an earlier layer would arrive at the same time with low-latitude emission from a later layer.

In order to analytically treat the problem, some assumptions still need to be made. One important parameter is the Lorentz factor Γ of each layer. According to the standard fireball model (Mészáros et al. 1993; Piran et al. 1993; Kobayashi et al. 1999), Γ should initially increase with radius before coasting to a certain value. The coasting Γ depends on a comparison between the dimensionless entropy of the fireball η and a critical value η_c (Mészáros & Rees 2000). If $\eta < \eta_c$, the photosphere radius r_{ph} is above the saturation radius $r_s = \eta r_0$ (where r_0 is the radius of the central engine), and the Lorentz factor coasts to a constant value $\Gamma_0 = \eta$. For $\eta > \eta_c$, the photosphere occurs during the fireball acceleration phase ($r_{ph} < r_s$). The Lorentz factor Γ would vary significantly across r_{ph} , which is difficult to handle

analytically. In our treatment, we have made the assumption of a constant Γ_0 throughout the shell evolution (i.e. the acceleration phase is neglected). In our model, for a certain layer although all the positions have a certain probability to release the last-scattered photon, the maximum probability is concentrated around the photosphere radius r_{ph} . So our calculation of the emerging photosphere spectrum based on the assumption of a constant Γ_0 is accurate enough as long as $r_{ph} \gg r_s$, but would become progressively inaccurate as r_{ph} becomes progressively smaller. In our calculations, this constraint is considered in care, so that the presented spectra are all in the regime where this assumption is valid.

3. MODELS & RESULTS

In this section, we calculate the photosphere spectra by progressively including the four new physical ingredients as discussed above. In §3.1 we introduce a blackbody spectrum in the comoving frame, while still keeping the basic assumptions of Pe’er & Ryde (2011) such as a constant wind luminosity, infinity outer boundary and single layer emission. In §3.2 we introduce multiple layers to study the superposed spectrum. In §3.3, keeping the wind luminosity constant, we introduce a time-evolving outer boundary of the outflow. In §3.4 we introduce a time-dependent wind luminosity and time-evolving outer boundary of the outflow at the same time. A discussion on E_p evolution patterns are presented in §3.5.

3.1. Impulsive injection, outer boundary at infinity, blackbody distribution of photons

In this section we still keep most simplifications made by Pe’er & Ryde (2011), including instantaneous injection of photons and an outer boundary at infinity. One modification is that we relax the δ -function assumption of photon energy (Pe’er 2008; Pe’er & Ryde 2011), but introduce a more realistic co-moving blackbody spectrum.

We start with the formula of Pe’er & Ryde (2011) that calculates the specific flux:

$$F_\nu(\nu, t) = \frac{N_0}{4\pi d_L^2} \int \int P(r, \theta) k_B T(r, u) \times \delta\left(t - \frac{ru}{\beta c}\right) \delta\left(\nu - \frac{k_B T'(r)}{h\Gamma u}\right) dudr \quad (1)$$

where N_0 is the impulsively injected number of photons at $t = 0$, $P(r, \theta)$ is the probability density function for the last scattering to occur at the radius r and to an angle θ , respectively, and the parameter

$$u = 1 - \beta \cos \theta \quad (2)$$

contains the angular information.

For the probability density function $P(r, \theta)$, Pe’er & Ryde (2011) used two independent functions $P(r)$ (for the radial dimension) and $P(u)$ (for the angular dimension) to decompose $P(r, \theta)$ into $P(r, \theta) = P(r) \cdot P(u)$, where

$$P(r) = \frac{r_{ph}}{r^2} e^{-\frac{r_{ph}}{r}} \quad (3)$$

where r_{ph} is the classical photosphere radius ($\tau = 1$) at $\theta = 0$, and

$$P(u) = \frac{1}{2\Gamma^2 \beta u^2}. \quad (4)$$

On the other hand, the simulation result in Pe'er & Ryde (2011) indicated that $P(r)$ depends on angle and $P(u)$ also depends on radius. Beloborodov (2011) later introduced a two dimensional $P(r, \theta)$ function based on the assumption of outer boundary at infinity:

$$\frac{dP}{drd\mu} = \mathcal{D}^2 \frac{r_{\text{ph}}}{4r^2} \left\{ \frac{3}{2} + \frac{1}{\pi} \arctan \left[\frac{1}{3} \left(\frac{r_{\text{ph}}}{r} - \frac{r}{r_{\text{ph}}} \right) \right] \right\} \exp \left[-\frac{r_{\text{ph}}}{6r} \left(3 + \frac{1 - \mu'}{1 + \mu'} \right) \right], \quad (5)$$

where $\mu' = \cos\theta'$ is in the outflow comoving frame, $\mu = \cos\theta$ is in the observer frame, and the Doppler factor is

$$\mathcal{D} = [\Gamma(1 - \beta \cos\theta)]^{-1} = (\Gamma u)^{-1}. \quad (6)$$

In this section and §3.2, we will use Eq.5 as $P(r, \theta)$ in Eq.1.

The last δ function in Eq.1 made the mono-energetic simplification for the photosphere photons. We consider a blackbody distribution of the photon energy and replace Eq.1 by a new equation

$$F_\nu(\nu, t) = \frac{N_0}{4\pi d_L^2} \int \int P(r, \mu) P(\nu, T) h\nu \times \delta \left(t - \frac{ru}{\beta c} \right) d\mu dr, \quad (7)$$

where we have defined a new parameter

$$P(\nu, T) = \frac{n_\gamma(\nu, T)}{\int_0^\infty n_\gamma(\nu, T) d\nu} = \frac{n_\gamma(\nu, T)(hc)^3}{16\pi\zeta(3)(kT)^3}, \quad (8)$$

which is the probability function of a photon with frequency ν in a Plank distribution with a temperature T at the coordinate (r, θ) as observed by an observer located at $\theta = 0$, and

$$n_\gamma(\nu, T) = \frac{8\pi\nu^2}{c^3} \frac{1}{\exp(h\nu/kT) - 1} \quad (9)$$

is the specific photon number density at frequency ν for an observed temperature T . Here the mathematical relation

$$\int_0^\infty \frac{x^2 dx}{e^x - 1} = 2\zeta(3) = 2 \times 1.202... \quad (10)$$

has been applied when calculating the integration $\int_0^\infty n_\gamma(\nu, T) d\nu$. Notice that here we have also adopted a blackbody function for the observed spectrum at any spatial point (r, θ) . This is justified, since for any spatial point, the spectral shape is not modified from that in the co-moving frame, except that the entire spectrum is Doppler boosted by the local Doppler factor (Li & Sari 2008). The global observed spectrum deviates from a blackbody due to different Doppler factors at different points. This effect is fully incorporated in our calculations.

The observer frame temperature at point (r, θ)

$$T(r, \theta) = \mathcal{D}T'(r) \quad (11)$$

depends on the angle through the Doppler factor and on the co-moving temperature. The co-moving frame temperature $T'(r)$ is more intrinsic, which depends on the radius r only. Its expression depends on the radius

range (Mészáros & Rees 2000), and can be calculated using the on-axis observed temperature divided by the on-axis Doppler factor $\mathcal{D}(\theta = 0) = 2\Gamma$, i.e.

$$T'(r) = T(r, \theta = 0)/(2\Gamma) = \begin{cases} T_0/(2\Gamma), & r < r_s < r_{\text{ph}}, \\ T_0(r/r_s)^{-2/3}/(2\Gamma), & r_s < r < r_{\text{ph}}, \\ T_0(r_{\text{ph}}/r_s)^{-2/3}/(2\Gamma), & r_s < r_{\text{ph}} < r, \end{cases} \quad (12)$$

where

$$T_0 = \left(\frac{L_0}{4\pi r_0^2 c a} \right)^{1/4} \quad (13)$$

is the temperature at the central engine, L_0 is the initial luminosity deposited at the central engine, and $r_0 = 10^7 r_{0,7}$ is the central engine radius. Notice that in order to satisfy our constant Γ assumption (§2.2), we have limited our study in the regime $r_s < r_{\text{ph}}$. Also for an easy treatment, in the above analytical model $T'(r)$ is taken as a broken power law function of r , whereas in reality it is a smoothly connected broken power law (Pe'er 2008).

Since we mostly care about the shape of the spectrum, the normalization parameter N_0 is approximately taken as

$$N_0 = \frac{E_0}{kT_0}, \quad (14)$$

which denotes the rough total number of photons released at the central engine (assuming mono-energetic photon energy). By doing so, we have assumed that no additional emission or absorption processes occur as the photon-mediated outflow travels from the central engine to the photosphere, and that photons only undergo Thomson scattering with the total number conserved.

We integrate Eq. 7 to calculate the instantaneous spectra at different times. The angle θ is integrated from 0 to $\pi/2$, which is wide enough to catch the relativistically beamed emission. The range of r is defined by the equal-arrival-time equation

$$t = \frac{ru}{\beta c}. \quad (15)$$

The results are presented in Fig.2. For an impulsive fireball as studied in this subsection, we calculate T_0 by taking $L_0 = 10^{52} \text{ erg s}^{-1}$, while adopt the impulsively injected total wind energy $E_0 = 10^{52} \text{ erg}$. This is to keep consistency with the continuous-wind calculations in the later subsections. Other parameters are adopted with the following values: dimensionless entropy $\eta = \Gamma = 300$, luminosity distance of the GRB $d_L = 2 \times 10^{28} \text{ cm}$ ($z \sim 1$), and the inner boundary of integration set to $r_0 = 10^7 \text{ cm}$.

From Fig.2, we can see that under the assumptions adopted in this subsection, the on-axis, instantaneous photosphere spectrum evolves from a pure blackbody (early on) to a gradually flattened shape as the high-latitude emission becomes progressively dominant. Compared with the analytical results of Pe'er & Ryde (2011), our results show an exponential tail of blackbody emission instead of the flat spectrum $F_\nu \propto \nu^0$ extending

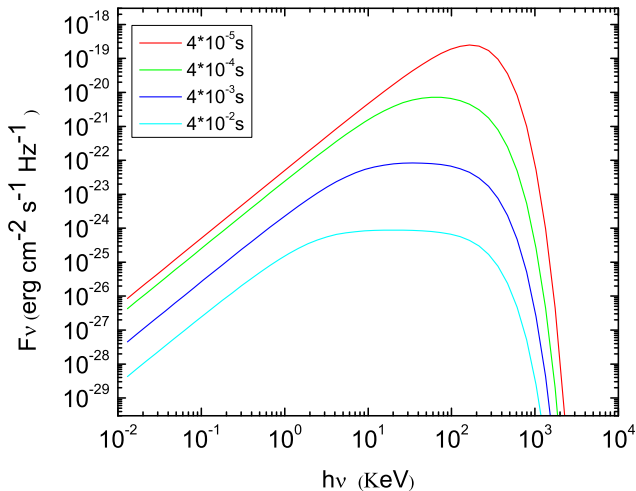


FIG. 2.— Instantaneous photosphere spectra for a fireball with impulsive injection of energy. The impulsively injected total energy is $E_0 = 10^{52}$ erg, the fireball temperature is calculated by taking $L_0 = 10^{52}$ erg s $^{-1}$, central engine radius $r_0 = 10^7$ cm, dimensionless entropy $\eta = \Gamma_0 = 300$, and luminosity distance $d_L = 2 \times 10^{28}$ cm. Different colors represent different observational times. The spectra become progressively high-latitude dominated all the way to high energies. Our results are however generally consistent with the numerical results of Pe'er & Ryde (2011).

3.2. Continuous wind with a constant wind luminosity and Lorentz factor

The next step is to study the observed instantaneous spectra for a continuous wind. For simplicity, we assume that the central engine wind has a constant luminosity and baryon loading rate, and hence, a constant Lorentz factor:

$$\begin{aligned} L_w(\hat{t}) &= L_0, \\ \dot{M}(\hat{t}) &= \dot{M}_0, \\ \eta(\hat{t}) &= \Gamma(\hat{t}) = \Gamma_0, \end{aligned} \quad (16)$$

where \hat{t} denotes the central-engine time since the injection of the very first layer of the wind.

In order to calculate the emission from the entire wind, we dissect the wind into many thin layers, with each layer denoted by its injection time \hat{t} . Repeating the excise discussed in §3.1, we can write the contribution of specific flux at the observer time t for a layer ejected during the time interval from \hat{t} to $\hat{t} + d\hat{t}$ (for $\hat{t} < t$)

$$\begin{aligned} \hat{F}_\nu(\nu, t, \hat{t}) &= \frac{\dot{N}_0(\hat{t})}{4\pi d_L^2} \int \int P(r, \mu) P(\nu, T) h\nu \\ &\times \delta\left(t - \hat{t} - \frac{r\mu}{\beta c}\right) d\mu dr. \end{aligned} \quad (17)$$

The δ -function here takes into account the retardation effect for different layers ejected at different injection time \hat{t} . The parameter $\dot{N}_0(\hat{t})$ is the instantaneous injection rate of photons at the central engine time \hat{t} , and a rough normalization

$$\dot{N}_0(\hat{t}) = \frac{L_w(\hat{t})}{kT(\hat{t})} \quad (18)$$

is adopted. The calculation of $T(\hat{t})$ follows Eqs. (12) and (13), with L_0 replaced by $L_w(\hat{t})$. Notice that the parameter \hat{F}_ν has the dimension of specific flux over time.

The total observed instantaneous specific flux at t can be obtained by integrating \hat{F}_ν over all the layers, i.e.

$$F_\nu(\nu, t) = \int_0^t \hat{F}_\nu(\nu, t, \hat{t}) d\hat{t}. \quad (19)$$

We study two cases in the following. In the first case, we assume that the central engine continuously injects an outflow with a constant luminosity during all the observation times (Fig.3). In the second case, we introduce shut-down of the central engine after a certain duration time (Fig.4 and Fig.5). All the parameters are the same as the ones adopted in §3.1, except E_0 is no longer used, and $L_w(\hat{t}) \equiv L_0 = 10^{52}$ erg s $^{-1}$ has been adopted.

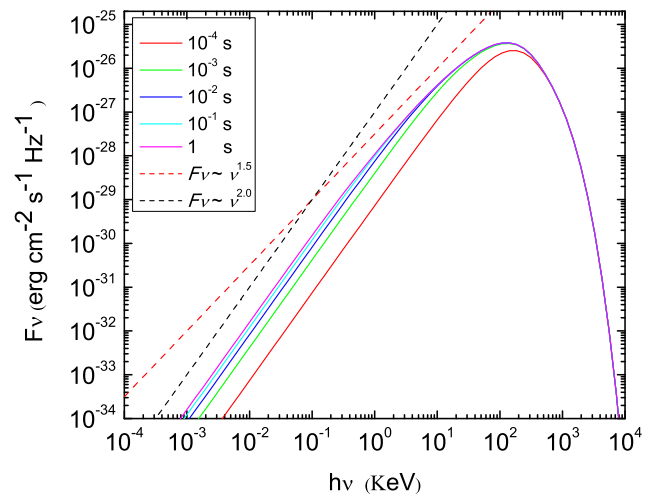


FIG. 3.— The instantaneous photosphere spectra of a continuous wind. The parameters are the same as Fig.2 except E_0 is not used and $L_w(\hat{t}) \equiv L_0 = 10^{52}$ erg s $^{-1}$ is adopted. The two dashed lines are the reference lines for $F_\nu \propto \nu^2$ (black) and $F_\nu \propto \nu^{1.5}$ (red), respectively.

Figure 3 presents the observed instantaneous photosphere spectra of a continuous wind with a constant luminosity and Lorentz factor. One can see several interesting features. The instantaneous spectrum is initially ($t = 10^{-4}$ s) blackbody-like with $F_\nu \propto \nu^2$ below the peak (Rayleigh-Jeans regime). Soon after, the spectrum below the peak starts to flatten, and a new segment with $F_\nu \propto \nu^{1.5}$ starts to merge below the peak. The reason for this softening can be understood from the results presented in Fig.2, which delineates the time evolution of instantaneous spectra of each layer. An old layer is high-latitude dominated, so that a more extended plateau with $\hat{F}_\nu \propto \nu^0$ spectral segment shows up. A relatively newer layer has a shorter plateau, and the newest layer has no plateau. The superposition of emission from all these layers give rise to relatively softer spectral segment. The spectral index of this new segment ($F_\nu \propto \nu^{1.5}$) is consistent with the result of Beloborodov (2010), who obtained a similar spectral index using a different method.

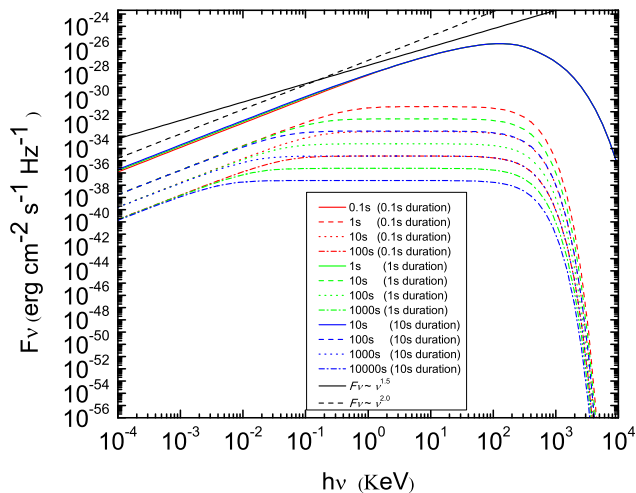


FIG. 4.— The instantaneous photosphere spectra of a continuous wind, which shuts down at a particular time. Parameters are same as Fig.3. Different color groups represent the spectra for different shut-down times: 0.1 s (red), 1 s (green) and 10 s (blue). For each group, four instantaneous spectra with different observation times are plotted: solid (end of continuous wind), dashed (one order of magnitude after), dotted (two orders of magnitude after) and dash-dotted (three orders). The two black lines are the reference lines for spectral indices being 2 and 1.5.

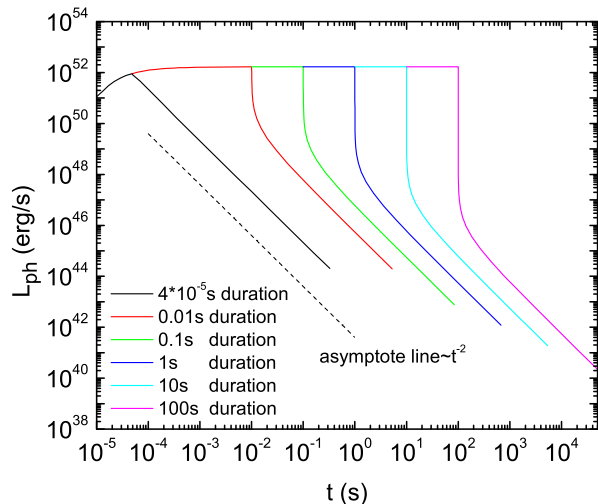


FIG. 5.— Photosphere luminosity light curves for continuous winds with abrupt shut-down of the central engine. Different colors represent different shut-down times. For the cases with duration longer than the characteristic duration ($t_N \sim 4 \times 10^{-5}$ s), the light curves initially fall rapidly before entering the t^{-2} phase. The longer the central engine time, the more significant the rapid drop is.

Notice that in Fig.3 the absolute flux increases with time. This is because at early epochs, the outmost layer only reaches a certain r above which no photons are released. Given a simplistic probability function defined in Eq.3 or Eq.5, a good fraction of photons do not contribute to the observed flux. In the following (§3.3), we will give a more accurate treatment on this effect.

Figure 4 presents the instantaneous photosphere spec-

tral evolution with the assumption that central engine shuts down after a certain duration. We calculate three different central engine durations: 0.1s (red group curves), 1s (green group curves) and 10s (blue group curves). For each case, we calculate four instantaneous spectra with different observational times: solid line (end of constant luminosity injection), dashed line (one order of magnitude in time after the injection phase), dotted line (two orders of magnitude after) and dash-dotted line (three orders of magnitude after). The results show that the shape of the spectrum become high-latitude dominated at later times, but early on there is a rapid falling phase. In order to fully reveal this feature, we calculate the photosphere luminosity evolution with time (light curve) as shown in Fig.5. Our results show that the luminosity evolution depends on the duration of the central engine. Even though at late times the decaying slope of L_{ph} is t^{-2} , shortly after wind terminates, L_{ph} decays rapidly like free-fall³. The longer of the central engine duration, the more significant the initial rapid drop it is. Only when the duration becomes as short as a characteristic duration t_N (Pe'er & Ryde 2011) $\sim r_{ph}/(2\Gamma^2c) \sim 4 \times 10^{-5}$ s, does the rapid falling phase disappear (black curve in Fig.5. This feature is caused by the “initial time effect” for log-log plots (see also Figure 3 of Zhang et al. (2006) in the case of afterglow emission). Previously Ryde & Pe'er (2009) analyzed the data from 56 long GRBs. They found that the light curves decay rate is universally around t^{-2} . They considered this as consistent with the prediction of the high latitude emission of the photosphere model. Our results in Fig.5 suggest that this interpretation is unlikely, since there is no steep decay phase (4 orders of magnitude drop in flux for a 1 s wind) observed.

3.3. Continuous wind with a constant wind luminosity, variable finite outer boundary

So far we have assumed that the outer boundary of the outflow is at infinity. For a constant luminosity wind, the optical depth at a certain position in the outflow is time independent. However, in real situations invoking a short, variable wind from a GRB, the outer boundary is time variable. As a result, the optical depth at a certain position in the outflow is time dependent and changes rapidly with time at early epochs due to the relativistic motion of the outflow, especially during the early phase of wind injection. Since the optical depth is one of the key factors to decide the photosphere probability function, the probability function also becomes time dependent. This also affects the observed photosphere temperature, and the observed E_p evolution in the photosphere model.

Technically, since our model is limited to the $r_{ph} > r_s$ case, in our calculation we keep track the evolution of r_{ph} and compare it with r_s , to make sure the presented results are relevant ones when $r_{ph} > r_s$ is satisfied. The assumption of constant luminosity and Lorentz factor (Eq.16) is still adopted in the calculations.

3.3.1. Optical depth calculation

³ Notice that the calculated photosphere luminosity slightly deviates from the input wind luminosity $L_0 = 10^{52}$ erg s⁻¹. This is caused by the inaccurate estimate of the normalization parameter N (Eq.18).

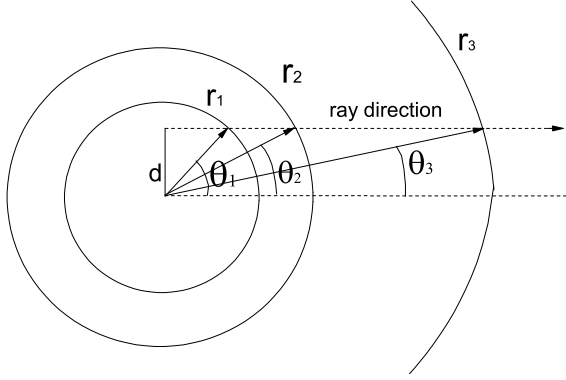


FIG. 6.— Geometric relations of the catch-up process.

For a wind with boundary at infinity, the optical depth can be written as (Abramowicz et al. 1991; Beloborodov 2011):

$$\begin{aligned}\tau &= \int_{r_1}^{\infty} d\tau \\ &= \int_{r_1}^{\infty} \mathcal{D}^{-1} \sigma_{\text{T}} n' ds \\ &= \int_{r_1}^{\infty} \mathcal{D}^{-1} \sigma_{\text{T}} n' dr / \cos \theta,\end{aligned}\quad (20)$$

where r_1 is the photon emission radius, ds and dr are along the ray direction and radial direction, respectively, $\mathcal{D} = [\Gamma(1 - \beta\mu)]^{-1}$ is the doppler factor and

$$n' = \frac{\dot{M}}{4\pi m_{\text{p}} \beta c \Gamma r^2} \quad (21)$$

is the number density in the comoving frame. Since the number density in rest frame is

$$n = \Gamma n', \quad (22)$$

the above equation can be written as

$$\begin{aligned}\tau &= \int_{r_1}^{\infty} \Gamma(1 - \beta\mu) \sigma_{\text{T}} n' dr / \cos \theta \\ &= \int_{r_1}^{\infty} (1 - \beta\mu) \sigma_{\text{T}} n dr / \cos \theta.\end{aligned}\quad (23)$$

For an finite outer boundary we are considering, the upper limit of integration has to be modified to a finite value. Assuming that a photon is emitted at a position (r_1, θ_1) , ahead of which there is a shell of materials extending to an outer boundary at r_2 (Fig.6). The light ray intersects with the out boundary of the shell at (r_2, θ_2) . Since the shell is also expanding near speed of light, the location as the photon catches up with the front of the shell would be at (r_3, θ_3) . The optical depth should then

be calculated by

$$\begin{aligned}\tau &= \int_{r_1}^{r_3} d\tau \\ &= \int_{r_1}^{r_3} (1 - \beta\mu) \sigma_{\text{T}} n dr / \cos \theta,\end{aligned}\quad (24)$$

where r_3 can be solved through the equations

$$r_3 \cos \theta_3 - r_1 \cos \theta_1 = c \Delta t_c, \quad (25)$$

and

$$r_3 - r_2 = \beta c \Delta t_c, \quad (26)$$

where Δt_c is the time for the photons emitted from (r_1, θ_1) to catch up with the outer boundary at (r_3, θ_3) . Meanwhile, a simple geometrical formula gives

$$d = r_1 \sin \theta_1 = r_2 \sin \theta_2 = r_3 \sin \theta_3, \quad (27)$$

where d is the distance between the line of ray and the axis of the explosion along line-of-sight (Fig.6).

These equations can be solved in two different ways. First, we can calculate the catching-up outer boundary position r_3 based on the initial value of r_1 , θ_1 and r_2 . The solution is:

$$r_3 = \Gamma^2 (-\mathcal{A} + \sqrt{\mathcal{A}^2 - (\mathcal{A}^2 + \beta^2 d^2) / \Gamma^2}), \quad (28)$$

where $\mathcal{A} = \beta r_1 \cos \theta_1 - r_2$. Here only one physical solution of r_3 (two mathematic solutions) is kept.

Second, one can solve for r_2 using r_3 , i.e.

$$\begin{aligned}r_2 &= r_3(1 - \beta \cos \theta_3) + \beta r_1 \cos \theta_1, \\ &= r_3(1 - \beta \sqrt{1 - \frac{d^2}{r_3^2}}) + \beta r_1 \cos \theta_1, \\ &= r_3 - \beta \sqrt{r_3^2 - d^2} + \beta r_1 \cos \theta_1.\end{aligned}\quad (29)$$

By employing $r_2 = r_1 + \beta c \delta \hat{t}$, one can find out $\delta \hat{t}$, which is the emission time difference between layers at position r_2 and r_1 . This second approach is applied during integration when a variable wind luminosity is introduced (see details in §3.4).

3.3.2. Modified probability function

With a finite outer boundary, one needs to modify the probability function of last scattering from the simple form with the infinite boundary (Eqs.(3-5)). In this subsection we develop a general method to calculate the probability function.

We first recall a simple radiation transfer model: $I = I_0 e^{-\tau}$, where I_0 is the initial radiation intensity and I is the observed intensity after absorption (scattering in the current case) with optical depth τ . So $I/I_0 = e^{-\tau}$ (which is $\sim \tau$ when $\tau \ll 1$) is the fraction of the remaining radiation flux, which would stand for the probability of not being scattered. The factor $1 - I/I_0 = 1 - e^{-\tau}$, on the other hand, stands for the probability of being scattered.

The probability function for last scattering can be calculated in three steps. First, the probability for a photon being scattered from radius r to $r + dr$ should be

$$P_r dr \propto d\tau = \sigma_{\text{T}} n(r) dr. \quad (30)$$

Second, the probability for the photon to be scattered to the observer's direction can be expressed as

$$P_{\Omega} d\Omega \propto -\frac{\mathcal{D}^2 d\mu d\phi}{4\pi} = \frac{\mathcal{D}^2 d\Omega}{4\pi}. \quad (31)$$

Here we have noticed that in the comoving frame of the flow, the probability to have the photon scattered to any direction is random, so that

$$P'_{\Omega'} d\Omega' \propto \frac{d\Omega'}{4\pi} = \frac{\sin\theta' d\theta' d\phi'}{4\pi} = -\frac{d\mu' d\phi'}{4\pi}, \quad (32)$$

$P'_{\Omega'} d\Omega' = P_{\Omega} d\Omega$, $d\mu' = \mathcal{D}^2 d\mu$, and $d\phi' = d\phi$. Finally, the probability for this scattered photon not being scattered again is $e^{-\tau}$. Putting everything together, one can write

$$P(r, \Omega) = \frac{\sigma_{\text{T}} n \mathcal{D}^2 e^{-\tau(r, \mu, r_{\text{out}})}}{4\pi A} \quad (33)$$

where the normalization factor is

$$\begin{aligned} A &= \int \int P(r, \Omega) dr d\Omega \\ &= \int_{r_{\text{min}}}^{r_{\text{max}}} \int_0^1 \int_0^{2\pi} \sigma_{\text{T}} n \frac{\mathcal{D}^2}{4\pi} e^{-\tau(r, \mu, r_{\text{out}})} dr d\mu d\phi \\ &= \int_{r_{\text{min}}}^{r_{\text{max}}} \int_0^1 \sigma_{\text{T}} n \frac{\mathcal{D}^2}{2} e^{-\tau(r, \mu, r_{\text{out}})} dr d\mu. \end{aligned} \quad (34)$$

Here the function $\tau(r, \mu, r_{\text{out}})$ is a function depending on r and μ , and the outer boundary r_{out} of the outflow at the time when the photon crosses the ejecta. It is r -dependent, and \hat{t} -dependent. The relation between r and r_{out} is the same as r_1 and r_3 discussed above (§3.3.1). Since this function is rapidly evolving with time, the probability function (Eq.(33)) is also rapidly evolving.

In the normalization function (Eq.(34)), the integration limits r_{min} and r_{max} should be 0 and $+\infty$, respectively. In reality, we take $r_{\text{min}} \sim r_0 = 10^7$ cm, and r_{max} a large enough number (e.g. 5×10^{17} cm). Since the probabilities at very small and very large distances are both very small. The actual numerical values of the two limits essentially do not affect the calculation results.

In Fig.7, we compare our probability function in the infinite outer boundary limit with those of Pe'er & Ryde (2011) and Beloborodov (2011). Our results agree with Pe'er & Ryde (2011) in the small angle limit ($\theta = 0$), and are more consistent with that of Beloborodov (2011) in the large angle limit ($\theta = 30^\circ, 60^\circ$).

3.3.3. Putting pieces together

The specific flux at time t for a layer ejected at the time \hat{t} can be expressed as

$$\begin{aligned} \hat{F}_{\nu}(\nu, t, \hat{t}) &= \frac{\dot{N}_0(\hat{t})}{4\pi d_L^2} \int \int \hat{P}(r, \Omega) P(\nu, T) h\nu \\ &\quad \times \delta\left(t - \hat{t} - \left(\frac{r\nu}{\beta c} - t_0\right)\right) d\Omega dr. \end{aligned} \quad (35)$$

Compared with the calculation in §3.2 (Eq.(17)), this expression has two improvements. First, we have introduced $t_0 = \frac{r_0}{\beta c(1+\beta)\Gamma^2}$ to reflect that the wind is ejected from a central engine with radius $r_0 = 10^7$ cm (instead

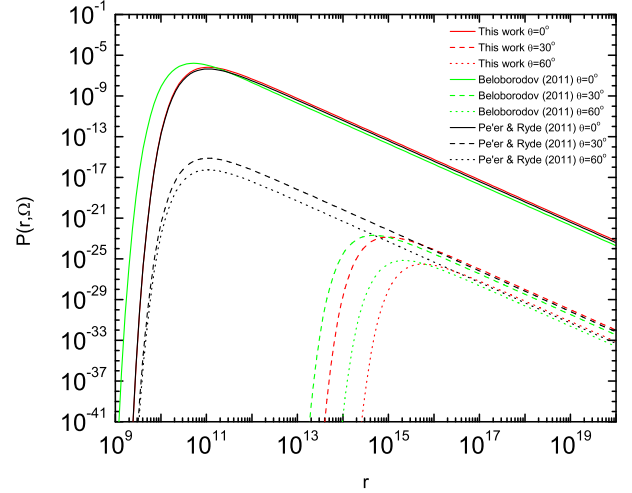


FIG. 7.— A comparison of the probability function $P(r, \Omega)$ between this work and those of Pe'er & Ryde (2011) and Beloborodov (2011).

of $r_0 = 0$). Second, since $P(r, \Omega)$ is no longer a universal function, we express it as $\hat{P}(r, \Omega)$ to specify that it is related to the layer ejected at \hat{t} . The expanded full expression of $\hat{F}_{\nu}(\nu, t, \hat{t})$ (Eq.(35)) is presented in the Appendix.

Again the instantaneous specific flux can be calculated by integrating the contributions from all layers

$$F_{\nu}(\nu, t) = \int_0^t \hat{F}_{\nu}(\nu, t, \hat{t}) d\hat{t}. \quad (36)$$

Finally, one can integrate over a time interval $[t_1, t_2]$ to get a time integral spectrum, which is what is observed:

$$F_{\nu}(\nu, t_1 \rightarrow t_2) = \int_{t_1}^{t_2} F_{\nu}(\nu, t) dt. \quad (37)$$

3.3.4. Results

Here, we present the calculation results for a constant wind luminosity with a variable outer boundary. The input parameters are: constant wind luminosity $L_w = 10^{52}$ erg s $^{-1}$, constant dimensionless entropy $\eta(\hat{t}) = \Gamma(\hat{t}) = \Gamma_0 = 300$, luminosity distance of the central engine $d_L = 2 \times 10^{28}$ cm ($z \sim 1$), and central engine radius $r_0 = 10^7$ cm.

Since our spectral calculation is valid for $r_{\text{ph}} > r_s$, we need to closely track the location of r_{ph} . Figure 8 shows the numerical results of r_{ph} evolution ($L_w = 10^{52}$ erg s $^{-1}$ and $\Gamma_0 = 300$). It shows that before 10^{-3} s, r_{ph} increases rapidly, while after 10^{-3} s, r_{ph} is nearly constant around 2×10^{11} cm. Since $r_s = \eta r_0 = 3 \times 10^9$ cm, the condition $r_{\text{ph}} > r_s$ is easily satisfied from very early time. We choose seven observer times, $10^{-6}, 10^{-5}, 10^{-3}, 0.5, 2.3, 10, 100$ seconds, to calculate the instantaneous spectra. The results are shown in Figure 9. We find that early on ($10^{-6} - 10^{-3}$ s), the spectra evolve rapidly. In particular, the temperature displays a strong hard-to-soft evolution. This is because initially the photosphere radius is closer in due to the less

opacity early on (Fig.8). However, such a phase is too short to have an observational consequence. After 10^{-3} s, the photosphere radius approaches the asymptotic value, so is the photosphere temperature. As a result, the last four spectra are nearly identical with minor differences in the low energy regime. In other words, there is essentially no temporal evolution with time. For a constant initial wind luminosity, the density and probability function for different layers are essentially the same. As a result, given a same r_{ph} the spectral behavior is rather similar. From the results, we find that the spectral index from 3 keV to the peak is modified from 2 to ~ 1.5 . This is again due to the superposition from the older layers' high latitude contribution, as already analyzed in §3.2. Compared with the results presented in §3.2 (which has an outer boundary at infinity), the more sophisticated method here can trace the evolution of the photosphere radius and probability function for a dynamic, finite outer boundary. For the constant luminosity case discussed in this sub-section, the finite boundary treatment makes a noticeable difference only at very early times ($t < 10^{-3}$ s). The difference is more obvious for a variable luminosity wind, as we discuss next.

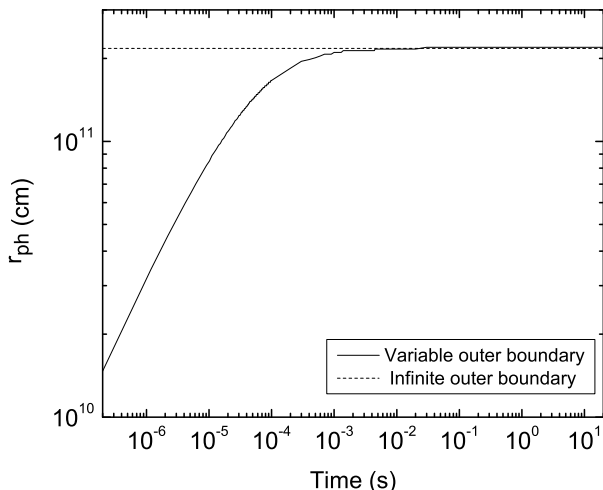


FIG. 8.— The evolution of r_{ph} as a function of observer time for a constant luminosity central engine wind. The dotted line is the asymptotic solution for an outer boundary at infinity.

3.4. Variable wind luminosity

In a real GRB, wind luminosity varies rapidly with time. Unlike the constant luminosity/ Γ model which preserves a $n \propto r^{-2}$ density profile of the wind, the density profile changes rapidly with time depending on the time history of luminosity, $L_w(\hat{t})$, and baryon loading, $\dot{M}(\hat{t})$. The integration for optical depth (Eq.(24)) becomes more complicated. In this sub-section, we develop a method to handle this problem. For simplicity, we assume a power law form of the time history, and assume a constant $\Gamma = \eta = L_w(\hat{t})/\dot{M}(\hat{t})c^2$ throughout.

3.4.1. Luminosity and baryon-loading history

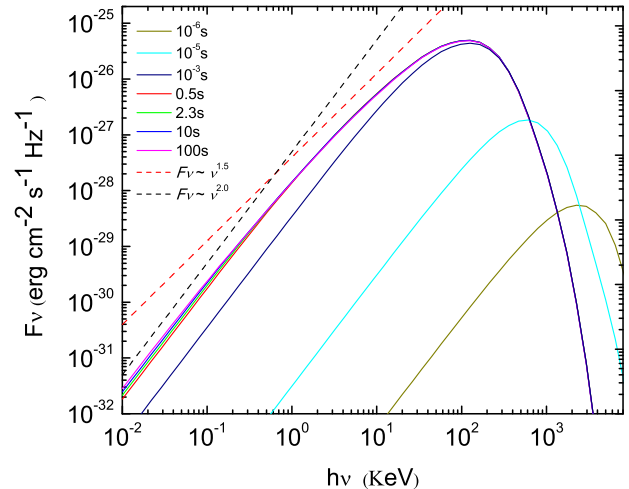


FIG. 9.— The instantaneous spectra for a constant luminosity wind with a variable outer boundary. Different colors stand for different epochs: 10^{-6} s (dark yellow), 10^{-5} s (cyan), 10^{-3} s (navy), 0.5 s (red), 2.3 s (green), 10 s (blue), and 100 s (magenta).

We approximate a GRB pulse as broken power law in luminosity, with rising and decaying indices as a_r and a_d , respectively, with a peak $L_{w,p}$ at \hat{t}_p . The luminosity history in the rising phase ($\hat{t} < \hat{t}_p$) can be written as

$$\log L_w(\hat{t}) = a_r \log \hat{t} + b_r, \quad (38)$$

while that in the decaying phase ($\hat{t} > \hat{t}_p$) can be written as

$$\log L_w(\hat{t}) = a_d \log \hat{t} + b_d, \quad (39)$$

where $b_r = \log L_{w,p} - a_r \log \hat{t}_p$ and $b_d = \log L_{w,p} - a_d \log \hat{t}_p$ are normalization parameters of the two power law segments.

3.4.2. Complications in the catch-up process

For the constant L_w and \dot{M} wind case as discussed in §3.3, since the n profile does not evolve with time, the integration of (24) from r_1 (photon emission radius) to r_3 (the radius where the photon escape the wind) is straightforward (see Fig.6 and §3.3.1 for detailed discussion). One can apply Eq.(28) to directly solve for r_3 given any r_2 , and the final optical depth is defined by the maximum catching up radius $r_{3,M}$ (which is also r_{out} discussed in §3.3.2) corresponding to the maximum $r_{2,M}$ of the wind at the time when the photon is emitted at r_1 .

In the variable wind case discussed here, since the n profile is variable with time, one needs to precisely determine n at any r_3 value in the range of $(r_1, r_{3,M})$. To do so, one needs to find out the corresponding r_2 of each r_3 using Eq.(29). Then one can connect r_2 with a certain central engine time \hat{t} , and hence, its baryon loading rate $\dot{M}(\hat{t})$, which defines the density profile, and hence, the relevant n at that r_3 .

Solving for Eq.(29), we find an interesting fact (Fig.10): at low latitudes with respect to the line-of-sight (small θ_1), r_2 is always larger than r_1 . This means that the emitted photons always catch up layers ejected earlier.

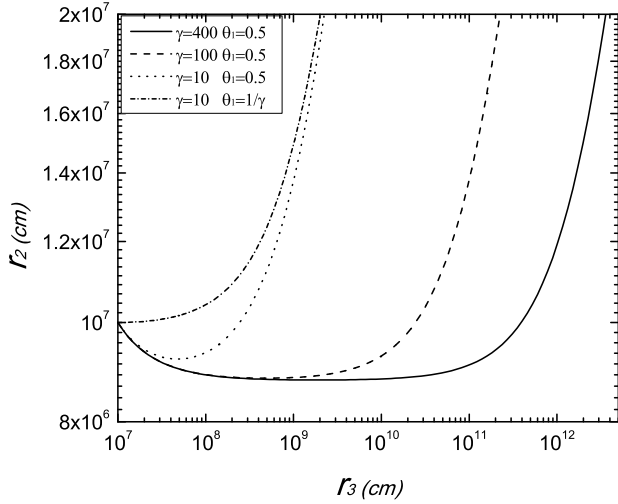


FIG. 10.— The relationship between r_2 and r_3 based on Equation (29). The solid, dashed, and dotted lines have the same initial angle $\theta_1 = 0.5$ but different Lorentz factors $\Gamma_0 = 400, 100$ and 10 . The dash-dotted line corresponds to the case of $\theta_1 = 1/\Gamma_0$ with $\Gamma_0 = 10$.

However, at large latitudes (large θ_1), r_2 can be smaller than r_1 . This means that photons emitted at a certain epoch would initially interact with the layers ejected later, so that it would see an even higher optical depth during propagation. This does not mean that the late ejected materials move with a superluminal velocity. A photon is caught up with by the electrons ejected later due to a geometric effect: electrons move in a hypotenuse “short-cut”, even though their bulk motion velocity is sub-luminal (Fig.6).

For a large-angle geometry when the reverse of r_2 and r_1 happens, the relationship between r_2 and r_3 shows an interesting feature. Performing derivative to equation (29), one gets

$$\frac{dr_2}{dr_3} = 1 - \frac{\beta r_3}{\sqrt{r_3^2 - d^2}} = 1 - \frac{\beta}{\cos \theta_3}. \quad (40)$$

Setting $dr_2/dr_3 = 0$, one gets a critical catch-up point $\cos \theta_3 = \beta$, or $\sin \theta_3 = 1/\Gamma_0$. In the early stages, θ_3 is relatively large, so that $\sin \theta_3 > 1/\Gamma_0$ and $dr_2/dr_3 < 0$ are satisfied. As a result, initially r_2 is smaller than r_1 (e.g. $\sim 10^7$ cm), and r_2 decreases when r_3 increases. After passing the critical point (Eq.40), dr_2/dr_3 becomes positive. The photon starts to overtake the outflow layers and eventually escape the wind. If the initial angle θ_1 is small enough from the beginning, i.e. $\sin \theta_1 < 1/\Gamma_0$ is satisfied from the beginning, r_2 would increase with r_3 all the time. In Figure (10), we show four different cases of $r_2 - r_3$ evolution. The solid, dashed, and dotted lines have the same initial angle $\theta_1 = 0.5$ but with different Lorentz factors. The dash-dotted line corresponds to the critical case $\theta_1 = 1/\Gamma_0$.

3.4.3. Optical depth calculation

With the above preparation, one can calculate optical depth of a photon in a variable-luminosity wind. Figure 11 shows the spacial distribution of wind luminosity at an instant t in the observer frame. The layers ejected at

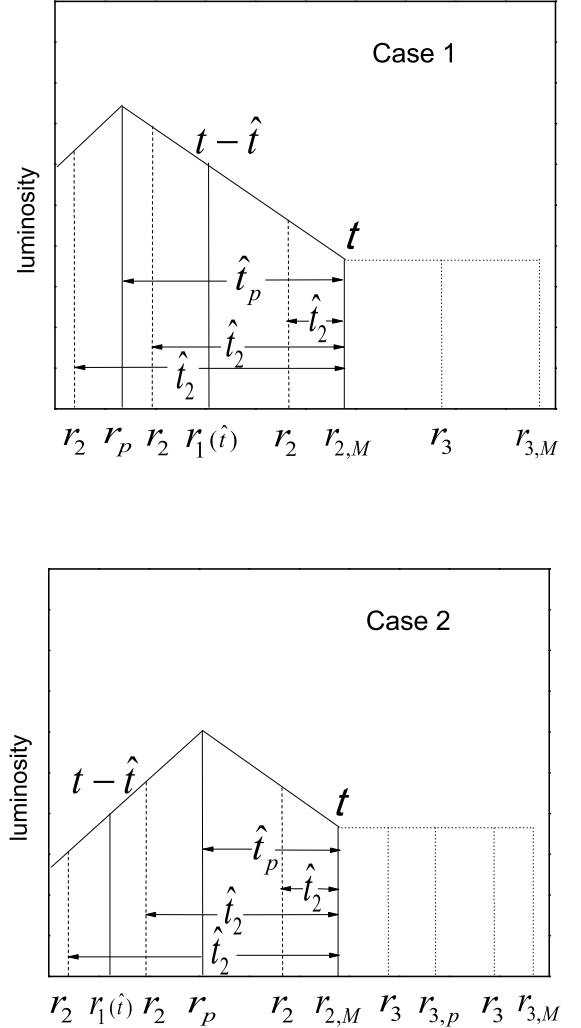


FIG. 11.— Instantaneous spacial structure of the wind luminosity as well as typical radii invoked to calculate optical depth.

an earlier epochs move in the front, so the spacial distribution is essentially a reversed temporal distribution. We have assumed a constant Lorentz factor in all layers so that the temporal profile does not evolve with time other than globally streaming forward.

We calculate the optical depth of a photon emitted from a layer ejected at the central engine time \hat{t} , which has an age of $t - \hat{t}$ at the observer time t . The radius of the layer is defined as r_1 (or more precisely $r_1(\hat{t})$). We discuss two cases in Fig.11: “Case 1” corresponds to the early stage when the photon is emitted during the rising phase of the pulse, while “Case 2” corresponds to the late stage when the photon is emitted during the falling phase. In both cases, the location of the layer emitted at the peak time \hat{t} is denoted as r_p .

At the time t when a photon is emitted at $r_1(\hat{t})$, all the layers emitted before \hat{t} are ahead of r_1 , and the maximum radius $r_{2,M}$ is the first layer ejected at $\hat{t} = 0$. The photon will over-take this layer at a much larger radius $r_{3,M}$. In order to calculate the optical depth of the photon τ ,

one needs to integrate Eq.(24) from r_1 to $r_{3,M}$. For any $r \in (r_1, r_{3,M})$ (r is effectively r_3), the density $n(r)$ is defined by its corresponding r_2 , which is related to $\hat{M}(\hat{t}_2)$ at the time

$$\hat{t}_2 = \frac{r_{2,M} - r_2}{\beta c}, \quad (41)$$

when the layer associated with r_2 was ejected. One therefore needs to solve for r_2 using Eq.(29) for every step in r (i.e. r_3).

In view of the complicated catch-up process discussed in §3.4.2, there are three possibilities for each case (Fig.11). For Case 1, one has $r_p < r_1 < r_2$, $r_p < r_2 < r_1$, or $r_2 < r_p < r_1$. The wind luminosity at \hat{t}_2 is defined by Eq.(38) for the first two cases, and by Eq.(39) for the last case. For Case 2, one has $r_1 < r_p < r_2$, $r_1 < r_2 < r_p$, or $r_2 < r_1 < r_p$. The wind luminosity at \hat{t}_2 is defined by Eq.(38) for the first case, and by Eq.(39) for the last two cases. From $L_w(\hat{t}_2)$ one can calculate $\hat{M}(\hat{t}_2) = L_w(\hat{t}_2)/\eta c^2$ given the constant η value, which can be used to calculate the density n using Equations (21) and (22). One can then complete integration to calculate the optical depth τ for any coordinate (r, θ) . The photosphere radius r_{ph}^θ at any angle θ is defined by the condition

$$\tau(r_{ph}^\theta, \theta) = \int_{r_{ph}}^{r_{3,M}} (1 - \beta \cos \theta) \sigma_T n dr / \cos \theta = 1. \quad (42)$$

And the traditional photosphere radius is defined as $r_{ph} = r_{ph}^{\theta=0}$.

3.4.4. Results

We perform calculations for several different luminosity profiles. We fix $L_{w,p} = 10^{52}$ erg s $^{-1}$, $\hat{t}_p = 2.4$ s, $\eta = \Gamma_0 = 300$, $r_0 = 10^7$ cm, and $d_L = 2 \times 10^{28}$ cm (effectively $z \sim 1$), and investigate six different luminosity profiles with $(a_r, a_d) = (+0.75, -1)$, $(+0.75, -2)$, $(+0.75, -5)$, $(+2, -1)$, $(+2, -2)$, $(+2, -5)$, respectively. Analytically, the on-axis ($\theta = 0$) photosphere radius (Mészáros & Rees 2000)

$$r_{ph} = \frac{L_w \sigma_T}{4\pi m_p c^3 \eta^3} \simeq 3.7 \times 10^{11} \text{ cm} L_{w,52} \eta_{2.5}^{-3} \quad (43)$$

follows the luminosity profile $L_w(\hat{t})$ for a constant η , so $r_{ph}(\hat{t})$ should follow the same temporal profile as $L_w(\hat{t})$. We numerically reproduced this for a variable luminosity wind, with a slight deviation only at very early epochs ($\hat{t} < 10^{-3}$ s). The saturation radius is $r_s = \eta r_0 = 3 \times 10^9$ cm ($\eta/300$). To assure $r_{ph} > r_s$, we choose the following observed epochs to calculate the instantaneous spectra: $t = 0.5$ s, 2.3 s before $\hat{t}_p = 2.4$ s, and $t = 2.5$ s, 4 s, and 10 s after \hat{t}_p . For $a_d = -5$ case, the last epoch ($t = 10$ s) already violates the $r_{ph} > r_s$ condition, so we do not include it in the calculation.

Figure 12 shows the calculated instantaneous spectra, each panel displaying results for a luminosity profile. For each panel, different colors show different epochs. We can see that during the rising phase ($t = 0.5, 2.3$ s) the resulting spectra are very similar to the cases for a constant luminosity (Fig.9), i.e. the spectral slope is modified from

Rayleigh-Jeans (2) to 1.5, mainly due to high-latitude contribution. During the decay phase ($t = 2.5, 4, 10$ s), the spectral index below E_p is somewhat shallower. This is because the high-latitude emission is more dominant since it comes from the layers that have higher luminosities. The steeper the decay phase, the more significant the high-latitude effect is.

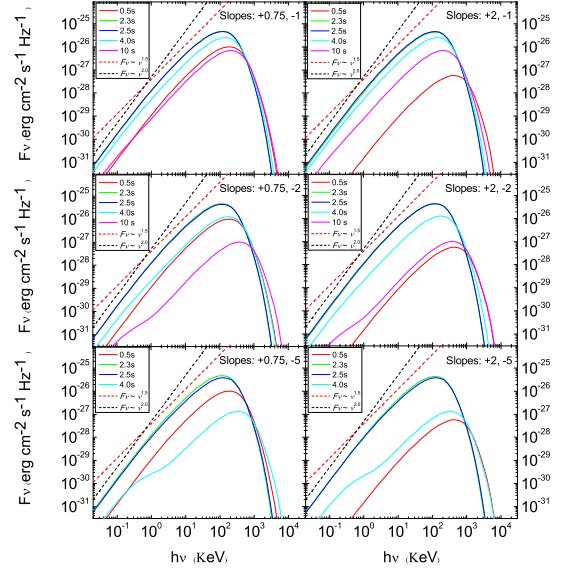


FIG. 12.— The instantaneous photosphere spectra of winds with variable luminosity. A constant $\Gamma_0 = 300$ and $d_L = 2 \times 10^{28}$ cm, a peak time $\hat{t}_p = 2.4$ s, and a peak luminosity $L_{w,p} = 10^{52}$ erg s $^{-1}$ are adopted for all cases. Different rising and decaying histories, and the temporal rising and decaying indices (slopes) are marked in each panel. For each panel, the spectra are calculated at the following times: 0.5 s (red), 2.3 s (green), 2.5 s (blue), 4 s (cyan), and 10 s (magenta). Two reference lines for spectral indices 1.5 (red dashed line) and 2 (black dashed line) are also drawn.

In Figure 13, we compare the resulting spectra for different Γ_0 . We fix $a_r = +0.75$, and vary a_d for three values -1, -2, -5. For each set of luminosity profile, we compare the resulting spectra for $\Gamma_0 = 300$ (solid curves) and $\Gamma_0 = 150$ (dashed curves). A smaller Γ_0 corresponds to a larger photosphere radius (Eq.(43)) and a lower photosphere temperature. A larger photosphere also gives a more significant high-latitude effect, which is reflected from the somewhat shallower spectral index below E_p during the decay phase, especially when a_d is steep.

Figure 14 shows the time integrated spectra. we choose 0.5 s as time bin for integration. For a same η and r_0 , the instantaneous spectra do not evolve significantly. As a result, the time-integrated spectra are not much different from the instantaneous ones.

We also consider the case when the variable luminosity central engine wind ceases abruptly. Still keeping the same parameters, but make the wind abruptly cease at

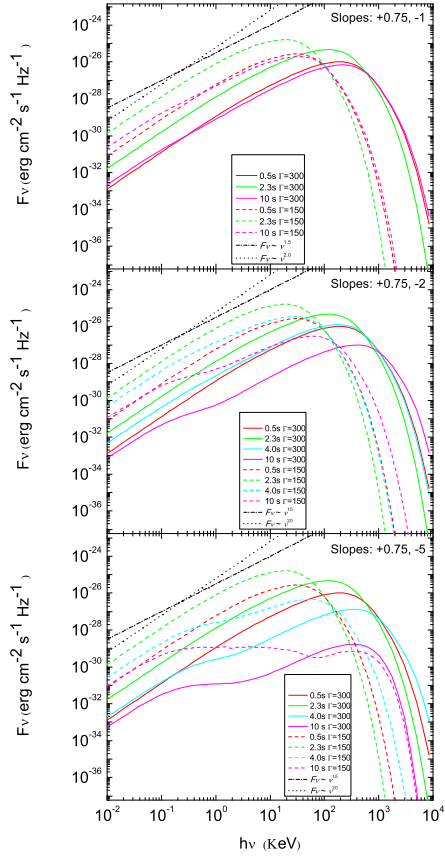


FIG. 13.— A comparison of instantaneous photosphere spectra for different Lorentz factors: $\Gamma_0 = 150$ (dashed) and 300 (solid). Other notations are the same as Fig.12.

$\hat{t}_p = 2.4$ s, the calculation spectra are presented in Fig.15. It is seen that at $t > \hat{t}_p$, a progressively more prominent plateau develops, similar to the results presented in Fig.4.

3.5. E_p evolution

The evolution of E_p is an important criterion to judge the correctness of a GRB prompt emission model. Observationally, hard-to-soft evolution and intensity-tracking patterns across a broad GRB pulse have been identified (Liang & Kargatis 1996; Ford et al. 1995; Lu et al. 2010, 2012), and some tracking behavior may be due to superposition of intrinsically hard-to-soft evolution pattern in most pulses (Hakkila & Prece 2011; Lu et al. 2012). It is important to check whether the quasi-thermal photosphere emission can reproduce the observed E_p evolution

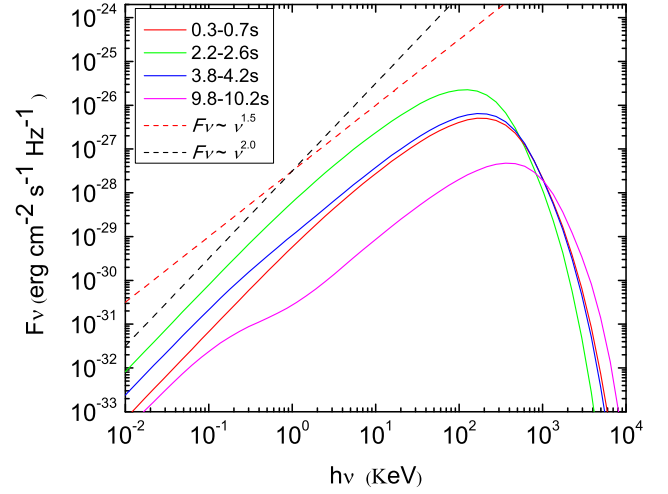


FIG. 14.— The time integrated photosphere spectra for the case “Slopes: +0.75, -2” with $\Gamma_0 = 300$. Integration in four time intervals are presented: 0.3-0.7 s (red), 2.2-2.6 s (green), 3.8-4.2 s (blue) and 9.8-10.2 s (magenta).

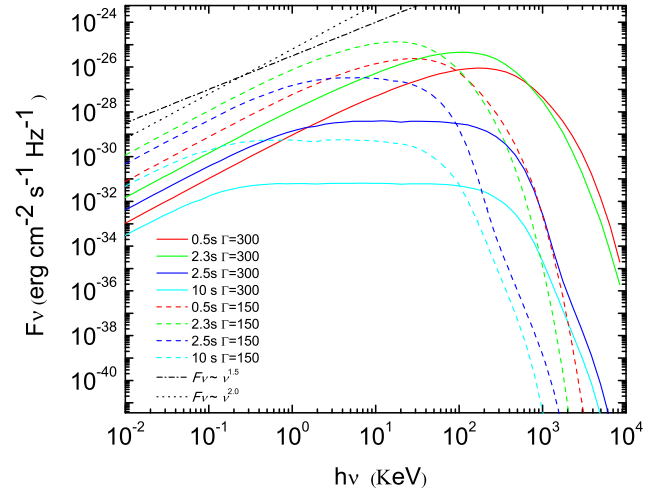


FIG. 15.— The instantaneous photosphere spectra for a variable luminosity wind with abrupt shut-down of the central engine. The parameters are the same as Fig.13, except there is a sharp cutoff at $\hat{t}_p = 2.4$ s. The dashed lines are for $\Gamma_0 = 150$, while the solid lines are for $\Gamma_0 = 300$. Different colors represent different observational times.

patterns.

Before performing numerical calculations, it is instructive to perform some analytical estimates. For the regime $r_{ph} > r_s$ we are interested in, one has $\eta = \Gamma_0$, $T_{ph} \propto L_w^{1/4} r_0^{-1/2} (r_{ph}/r_s)^{-2/3}$, $r_s = \eta r_0$, and $r_{ph} \sim L_w \eta^{-3}$, so that the observer temperature can be expressed as:

$$E_p \propto T_{ph} \propto L_w^{-5/12} r_0^{1/6} \eta^{8/3}. \quad (44)$$

One can immediately see that if η and r_0 are constants, E_p is anti-correlated to L_w . This trend seems to be consistent with the “hard-to-soft” evolution pattern during the pulse rising phase. However, it gives an opposite

trend during the pulse decaying phase, namely, E_p rises as luminosity drops. Based on the numerical results of instantaneous spectra presented in Fig.12, we plot E_p evolution with respect to wind and photosphere luminosities in Fig.16. The $L_w - E_p$ anti-correlation is clearly shown. Such a pattern has never been observed in GRB pulses.

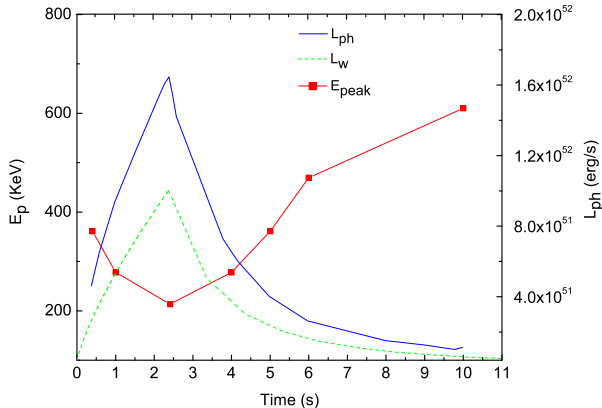


FIG. 16.— The evolution of E_p (Red solid line), initial wind luminosity L_w (green dash line), and the photosphere luminosity L_{ph} (blue solid line) for the case “Slopes: +0.75, -2”, $\Gamma_0 = 300$.

A related idea would be to attribute to the decaying phase as due to the high-latitude curvature effect. By doing so, one may expect to have E_p continues to decay during the decaying phase of the pulse. Including the $E_p - L_w$ anti-correlation during the rising phase, this might reproduce the observed hard-to-soft evolution pattern. In Fig.17, based on the numerical results of the instantaneous spectra presented in Fig.15, we plot E_p evolution with respect to wind and photosphere luminosities. As can be seen from the figure, this model also cannot reproduce the data. There are two problems: First, the high-latitude curvature tail of the photosphere luminosity light curve drops rapidly (similar to Fig.5), since the photosphere radius is small. The predicted E_p evolution during the tail (even though not measurable due to the rapid decay of the flux) displays a flat feature. This is because the upper end of the flat segment of the F_ν spectrum in the high-latitude-emission-dominated phase (which defines E_p) essentially does not decay with time (Fig.4).

If one allows η to vary with L_w with a certain power law dependence, the E_p -evolution pattern may be modified. From Eq.44, one can see that if one defines $\eta = L_w^m$, one would have $E_p \propto L_w^{(-5+32m)/12}$. The $E_p - L_w$ dependence would be reversed (i.e. positive dependence) when $m > 5/32 \simeq 0.156$. From afterglow data, Liang et al. (2010); Lü et al. (2012) have discovered a rough global $\Gamma_0 \propto L_w^{1/4}$ correlation in different GRBs. If such a correlation also exist within a same GRB, as theoretically motivated in GRB central engine models (Lei et al. 2013), then one would predict an $E_p - L$ intensity tracking be-

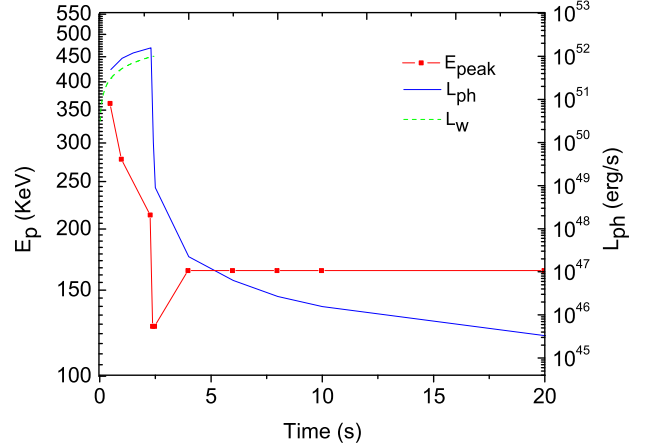


FIG. 17.— The evolution of E_p (Red solid line), initial wind luminosity L_w (green dash line), and the photosphere luminosity L_{ph} (blue solid line) for the case “Slope +0.75” with an abrupt shut-down and $\Gamma_0 = 300$.

havior within this simple photosphere model. Such a pattern has been observed in a fraction of GRB pulses (Lu et al. 2012). For the hard-to-soft evolution case, on the other hand, in order to reproduce the data, one has to demand that the index m switches from $m < 5/32$ before the peak to $m > 5/32$ after the peak. This requires contrived physical conditions that are not known theoretically.

4. CONCLUSIONS AND DISCUSSION

In this paper, we have developed a sophisticated method to calculate quasi-thermal GRB photosphere spectra numerically by introducing several improvements on previous treatments (Pe’er 2008; Pe’er & Ryde 2011). The new ingredients introduced in this paper include: the probability distribution of the location of a dynamically evolving photosphere, superposition of emission from an equal-arrival-time “volume” in a continuous wind, the evolution of optical depth of a wind with finite but evolving outer boundary, as well as the effect of different wind luminosity profiles. By assuming a co-moving blackbody spectrum emerging from the photosphere and a top-hat jet profile, we address how these effects modify the observed spectra from blackbody. The following robust conclusions are drawn: 1. For an outflow with constant or increasing wind luminosity, the low-energy spectrum below E_p can be modified to $F_\nu \sim \nu^{1.5}$, corresponding to a low-energy photon index $\alpha \sim +0.5$. Introducing temporal smearing does not change α significantly. 2. A softer spectrum can be obtained during the phase of decreasing wind luminosity with time, and a flat spectrum $F_\nu \sim \nu^0$ ($\alpha = -1$) can be obtained only when the spectrum is high-latitude emission dominated. However, since the photosphere radius is small, the flux drops very rapidly shortly after the wind terminates. 3. Depending on how η is related to L_w , this model can give both negative or positive $E_p - L_w$ correlation. The observed “hard-to-soft” evolution of E_p across broad pulses of seconds duration (Lu et al. 2012) cannot be interpreted with this simple photosphere model, unless an unknown contrived physical condition to switch the index m at the pulse peak is invoked. The intensity tracking patterns as ob-

served in some broad pulses (Lu et al. 2012) can be accounted for this model if $\eta \propto L_w^m$ with $m > 5/32$.

The results presented here suggest that the observed dominant spectral component, the so-called “Band-function” (Band et al. 1993) component, is not easy to interpret by this simplest photosphere model. The predicted low energy spectral index $\alpha = +0.5$ is too hard compared with the typical observed value ($\alpha = -1$), and the widely observed “hard-to-soft” E_p evolution across broad pulses cannot be accounted for unless a contrived condition is invoked. In order to naturally interpret GRB spectra within the framework of the photosphere model, more complicated factors have to be considered. One possibility is to introduce energy dissipation (e.g. proton-neutron collisions, internal shocks, or magnetic reconnections) and particle heating around the photosphere region. Such a dissipative photosphere model can naturally account for a high energy tail through Compton scattering, but could not significantly modify the low-energy spectral index from $\alpha \sim +0.5$. Vurm et al. (2011) introduced a synchrotron emission component, which peaks below the quasi-thermal component to make the “effective” low-energy spectral index softer. In order to make this synchrotron + quasi-thermal spectrum mimic a Band function as observed, the outflow magnetization parameter has to fall into a narrow range. Recently, Thompson & Gill (2013) invoked a magnetically dominated, low baryon-loading outflow, and modified the low-energy spectral index through the contribution from electron-positron pairs. Several authors pointed out the contrived conditions for the dissipative photosphere models to produce a single-component spectrum (Vurm et al. 2013; Asano & Mészáros 2013; Kumar & Zhang 2013). Another possibility to soften the spectrum below E_p is to introduce a structured jet. Lundman et al. (2013) showed that $\alpha \sim -1$ can be reproduced given that the GRB jets have a near constant L_w but a structured Lorentz factor profile with angle. This can enhance the high-latitude contribution (large $1/\Gamma$ cone at high-latitudes) to raise flux in large angles. For more general structured jets where both L_w and Γ follow a certain angular profile (e.g. Mészáros et al. 1998; Zhang & Mészáros 2002b; Rossi et al. 2002; Zhang et al. 2004), the α value would not be very different from what is calculated in this paper. In all these models, it is unclear how the “hard-to-soft” E_p evolution commonly

observed in many GRB pulses can be accounted for.

Alternatively, the main Band-component in the GRB spectra could arise from an optically-thin region well above the photosphere due to synchrotron radiation. Uhm & Zhang (2013) recently showed that if the emission radius is large enough, the fast cooling problem for synchrotron radiation is alleviated, and $\alpha \sim -1$ can be reproduced in a moderately fast cooling regime. The hard-to-soft E_p evolution pattern is a natural prediction in this model, since the outflow streams from small-radii where magnetic fields are stronger to large-radii where magnetic fields are weaker. Alternatively, the Band component may be interpreted as slow-cooling or slow-heating synchrotron emission in internal shocks where magnetic field strengths decays rapidly behind the shock (Pe’er & Zhang 2006; Asano & Terasawa 2009; Zhao et al. 2014).

Recent Fermi observations revealed a quasi-thermal component superposed on the main Band component in a growing population of GRBs (Ryde et al. 2010; Zhang et al. 2011; Guiriec et al. 2011; Axelsson et al. 2012; Guiriec et al. 2013). The spectral shape in our calculated photosphere emission is consistent with what is observed, suggesting that that component is very likely the photosphere emission from the GRB outflow (Pe’er et al. 2012). This component is typically weaker than what is predicted in the standard fireball-internal-shock model, so that a certain degree of magnetization is needed for the outflow (Zhang & Pe’er 2009). Within this picture, the non-thermal emission region in the optically-thin zone could be the internal shock region only if the magnetization parameter already falls below unity at the internal shock radius (Daigne et al. 2011). It is possible that the outflow is still moderately magnetically dominated in the large zone. In this case, efficient GRB emission is possible due to internal-collision-induced magnetic reconnection and turbulence (ICMART) (Zhang & Yan 2011; Zhang & Zhang 2014).

We thank Xue-Feng Wu, Asaf Pe’er, Andrei M. Beloborodov, Z. Lucas Uhm, He Gao, Wei-Hua Lei, Hou-Jun Lü, and Bin-Bin Zhang for helpful discussion or comments, and an anonymous referee for helpful suggestions. This work is partially supported by NASA under grant NNX10AD48G.

APPENDIX

Plugging in $P(\nu, T)$, $\hat{P}(r, \Omega)$ in Equation (35), one gets

$$\begin{aligned}
\hat{F}_\nu(\nu, t, \hat{t}) &= \frac{\dot{N}_0}{4\pi d_L^2} \int \int \hat{P}(r, \Omega) \cdot \frac{n_\gamma(\nu, T)}{16\pi(\frac{kT}{hc})^3 \cdot \zeta(3)} \cdot h\nu \cdot \delta\left(t - \hat{t} - \left(\frac{ru}{\beta c} - t_0\right)\right) d\Omega dr \\
&= \frac{\dot{N}_0}{4\pi d_L^2} \int_{r_{\min}}^{r_{\max}} \int_0^{2\pi} \frac{\sigma_T n' \Gamma \frac{D^2}{4\pi} e^{-\tau(r, \mu, r_{\text{out}})}}{A} \cdot \frac{n_\gamma(\nu, T)}{16\pi(\frac{kT}{hc})^3 \cdot \zeta(3)} \cdot h\nu \cdot \delta\left(t - \hat{t} - \left(\frac{ru}{\beta c} - t_0\right)\right) d(-\mu) d\phi dr \\
&= \frac{\dot{N}_0}{4\pi d_L^2} \int_{r_{\min}}^{r_{\max}} \frac{\sigma_T n' \Gamma \frac{D^2}{2} e^{-\tau(r, \mu, r_{\text{out}})}}{A} \cdot \frac{n_\gamma(\nu, T)}{16\pi(\frac{kT}{hc})^3 \cdot \zeta(3)} \cdot h\nu \cdot \delta\left(t - \hat{t} - \left(\frac{ru}{\beta c} - t_0\right)\right) d(-\mu) dr \\
&= \frac{\dot{N}_0}{4\pi d_L^2} \int_{r_{\min}}^{r_{\max}} \frac{\sigma_T n' \Gamma \frac{1}{2\beta(\Gamma u)^2} e^{-\tau(r, \mu, r_{\text{out}})}}{A} \cdot \frac{8\pi g^2 \frac{1}{c^3} \frac{1}{\exp(\frac{h\nu}{kT}) - 1}}{16\pi(\frac{kT}{hc})^3 \cdot \zeta(3)} \cdot h\nu \cdot \delta\left(u - \frac{\beta c(t - \hat{t} + t_0)}{r}\right) \frac{\beta c}{r} du dr \quad (u = 1 - \beta\mu) \\
&= \frac{\dot{N}_0}{4\pi d_L^2} \int_{r_{\min}}^{r_{\max}} \frac{\sigma_T n' \Gamma \frac{1}{2\beta(\Gamma u)^2} e^{-\tau(r, \mu, r_{\text{out}})}}{A} \cdot \frac{8\pi \nu^2 (\exp(\frac{h\nu \Gamma u}{kT'}) - 1)^{-1}}{16\pi(\frac{kT}{hc\Gamma u})^3 \cdot \zeta(3)} \cdot h\nu \cdot \delta\left(u - \frac{\beta c(t - \hat{t} + t_0)}{r}\right) \frac{\beta c}{r} du dr \quad (T = \frac{T'}{\Gamma u}) \\
&= \frac{\dot{N}_0}{4\pi d_L^2} \int_{r_{\min}}^{r_{\max}} \frac{\sigma_T n' \Gamma \frac{r^2}{2\beta(\Gamma\beta c(t - \hat{t} + t_0))^2} e^{-\tau(r, \mu, r_{\text{out}})}}{A} \cdot \frac{2\nu^2 (\exp(\frac{h\nu\Gamma\beta c(t - \hat{t} + t_0)}{kT'r}) - 1)^{-1}}{4(\frac{kT'r}{hc\Gamma\beta c(t - \hat{t} + t_0)})^3 \cdot \zeta(3)} \cdot h\nu \frac{\beta c}{r} dr.
\end{aligned} \tag{1}$$

The limits of integration can be calculated from the formula of equal arrival time surface, $t - \hat{t} = \frac{ru}{\beta c}$, i.e. $r = \frac{\beta c(t - \hat{t})}{u}$. With $\theta_{\min} = 0$ and $\theta_{\max} = \pi/2$, we get $r_{\min} = \max[\beta c(t - \hat{t}), r_0]$ and $r_{\max} = \max[\frac{\beta c(t - \hat{t})}{1 - \beta}, r_0] = \max[\Gamma^2(1 + \beta)\beta c(t - \hat{t}), r_0]$.

REFERENCES

- Abramowicz, M. A., Novikov, I. D., & Paczynski, B. 1991, *ApJ*, 369, 175
- Asano, K., & Terasawa, T. 2009, *ApJ*, 705, 1714
- Asano, K., & Mészáros, P. 2013, *JCAP*, 9, 8
- Axelsson, M., Baldini, L., Barbiellini, G., et al. 2012, *ApJ*, 757, L31
- Band, D., Matteson, J., Ford, L., et al. 1993, *ApJ*, 413, 281
- Beloborodov, A. M. 2010, *MNRAS*, 407, 1033
- . 2011, *ApJ*, 737, 68
- Burgess, J. M., Preece, R. D., Baring, M. G., et al. 2011, *ApJ*, 741, 24
- Daigne, F., Bošnjak, Ž., & Dubus, G. 2011, *A&A*, 526, A110
- Daigne, F., & Mochkovitch, R. 1998, *MNRAS*, 296, 275
- Ford, L. A., Band, D. L., Matteson, J. L., et al. 1995, *ApJ*, 439, 307
- Gao, H., Zhang, B.-B., Zhang, B. 2012, *ApJ*, 748, 134
- Ghirlanda, G., Celotti, A., & Ghisellini, G. 2002, *A&A*, 393, 409
- Ghirlanda, G., Celotti, A., & Ghisellini, G. 2003, *A&A*, 406, 879
- Ghirlanda, G., Bosnjak, Z., Ghisellini, G., Tavecchio, F., & Firmani, C. 2007, *MNRAS*, 379, 73
- Ghirlanda, G., Nava, L., & Ghisellini, G. 2010, *A&A*, 511, A43
- Ghirlanda, G., Ghisellini, G., Nava, L., & Burlon, D. 2011, *MNRAS*, 410, L47
- Ghirlanda, G., Ghisellini, G., & Nava, L. 2011, *MNRAS*, 418, L109
- Ghirlanda, G., Pescalli, A., & Ghisellini, G. 2013, *MNRAS*, 432, 3237
- Ghisellini, G., & Celotti, A. 1999, *ApJ*, 511, L93
- Giannios, D. 2008, *A&A*, 480, 305
- Guiriec, S., Connaughton, V., Briggs, M. S., et al. 2011, *ApJ*, 727, L33
- Guiriec, S., Daigne, F., Hascoët, R., et al. 2013, *ApJ*, 770, 32
- Hakkila, J., & Preece, R. D. 2011, *ApJ*, 740, 104
- Hakkila, J., & Preece, R. D. 2014, *ApJ*, in press, arXiv:1401.4047
- Ioka, K. 2010, *Progress of Theoretical Physics*, 124, 667
- Kobayashi, S., Piran, T., & Sari, R. 1999, *ApJ*, 513, 669
- Kumar, P., & Narayan, R. 2009, *MNRAS*, 395, 472
- Kumar, P., & Panaitescu, A. 2008, *MNRAS*, 391, L19
- Kumar, P., & Zhang, B. 2013, *Phys. Rep.*, submitted
- Lazzati, D., & Begelman, M. C. 2010, *ApJ*, 725, 1137
- Lazzati, D., Morsony, B. J., Margutti, R., & Begelman, M. C. 2013, *ApJ*, 765, 103
- Lei, W.-H., Zhang, B., & Liang, E.-W. 2013, *ApJ*, 765, 125
- Li, C., & Sari, R. 2008, *ApJ*, 677, 425
- Liang, E., & Kargatis, V. 1996, *Nature*, 381, 49
- Liang, E.-W., Yi, S.-X., Zhang, J., et al. 2010, *ApJ*, 725, 2209
- Lloyd, N. M., & Petrosian, V. 2000, *ApJ*, 543, 722
- Lü, J., Zou, Y.-C., Lei, W.-H., et al. 2012, *ApJ*, 751, 49
- Lu, R.-J., Hou, S.-J., & Liang, E.-W. 2010, *ApJ*, 720, 1146
- Lu, R.-J., Wei, J.-J., Liang, E.-W., et al. 2012, *ApJ*, 756, 112
- Lundman, C., Pe'er, A., & Ryde, F. 2013, *MNRAS*, 428, 2430
- Mészáros, P., Laguna, P., & Rees, M. J. 1993, *ApJ*, 415, 181
- Mészáros, P., Ramirez-Ruiz, E., Rees, M. J., & Zhang, B. 2002, *ApJ*, 578, 812
- Mészáros, P., Rees, M. J. & Wijers, R. A. M. J. 1998, *ApJ*, 499, 301
- Mészáros, P., & Rees, M. J. 2000, *ApJ*, 530, 292
- Mészáros, P., Rees, M. J., & Papathanassiou, H. 1994, *ApJ*, 432, 181
- Mizuta, A., Nagataki, S., Aoi, J. 2011, *ApJ*, 732, 26
- Nava, L., Ghirlanda, G., Ghisellini, G., & Celotti, A. 2011, *A&A*, 530, A21
- Pe'er, A. 2008, *ApJ*, 682, 463
- Pe'er, A., Mészáros, P., & Rees, M. J. 2006, *ApJ*, 642, 995
- Pe'er, A., & Ryde, F. 2011, *ApJ*, 732, 49
- Pe'er, A., & Zhang, B. 2006, *ApJ*, 653, 454
- Pe'er, A., Zhang, B.-B., Ryde, F., McGlynn, S., Zhang, B., Preece, R. D., Kouveliotou, C. 2012, *MNRAS*, 420, 468
- Piran, T., Shemi, A., & Narayan, R. 1993, *MNRAS*, 263, 861
- Preece, R. D., Briggs, M. S., Malozzi, R. S., et al. 2000, *ApJS*, 126, 19
- Preece, R. D. et al. 2014, *Science*, 343, 51
- Rees, M. J., & Mészáros, P. 2005, *ApJ*, 628, 847
- Rossi, E., Lazzati, D., & Rees, M. J. 2002, *MNRAS*, 332, 945
- Ruffini, R., Siutsou, I. A., & Vereshchagin, G. V. 2013, *ApJ*, 772, 11
- Ryde, F. 2005, *ApJ*, 625, L95
- Ryde, F., & Pe'er, A. 2009, *ApJ*, 702, 1211
- Ryde, F., Axelsson, M., Zhang, B. B., et al. 2010, *ApJ*, 709, L172
- Tavani, M. 1996, *ApJ*, 466, 768
- Thompson, C. 1994, *MNRAS*, 270, 480

- Thompson, C., Mészáros, P., & Rees, M. J. 2007, ApJ, 666, 1012
Thompson, C., & Gill, R. 2013, ApJ, submitted (arXiv:1310.2480)
Toma, K., Wu, X.-F., & Mészáros, P. 2011, MNRAS, 415, 1663
Uhm, Z. L., & Zhang, B. 2013, arXiv:1303.2704
Veres, P., Zhang, B.-B., & Mészáros, P. 2012, ApJ, 761, L18
Vurm, I., Beloborodov, A. M., & Poutanen, J. 2011, ApJ, 738, 77
Vurm, I., Lyubarsky, Y., & Piran, T. 2013, ApJ, 764, 143
Wang, X., Li, Z., Dai, Z., & Mészáros, P. 2009, ApJ, 698, L98
Zhang, B., Dai, X., Lloyd-Ronning, M., & Mészáros, P. 2004, ApJ, 601, L119
Zhang, B., Fan, Y. Z., Dyks, J., et al. 2006, ApJ, 642, 354
Zhang, B., Lu, R.-J., Liang, E.-W., & Wu, X.-F. 2012, ApJ, 758, L34
Zhang, B., & Mészáros, P. 2002a, ApJ, 581, 1236
Zhang, B., & Mészáros, P. 2002b, ApJ, 571, 876
Zhang, B., & Pe'er, A. 2009, ApJ, 700, L65
Zhang, B., & Yan, H. 2011, ApJ, 726, 90
Zhang, B., & Zhang, B. 2014, ApJ, 782, 92
Zhang, B.-B., Zhang, B., Liang, E.-W., et al. 2011, ApJ, 730, 141
Zhao, X. H., Li, Z., Liu, X. et al. 2014, ApJ, 780, 12